Contribution to the System Design of Contactless Energy Transfer Systems

David Maier, Jörg Heinrich, Marco Zimmer, Marcel Maier, and Nejila Parspour

***Abstract*—In this contribution, a design procedure that is applicable to many kinds of wireless or contactless energy transfer systems is proposed. The design procedure is limited to near field wireless energy transfer systems in resonant operation. For this purpose, the input impedance and voltage transfer function of different natural frequencies are calculated analytically, and moreover, the behavior of the system is described. Following three issues lead to a readily applicable design procedure. First, the knowledge of the transfer functions. Secondly, the knowledge of basic magnetic properties and lastly, the known influence of harmonics according to rectifier and inverter. This design procedure is demonstrated with two hardware setups.**

***Index Terms*—Inductive charging, inductive power transmission, power conversion harmonics, resonant inverters, transfer functions.**

I. Introduction

In recent years, inductive contactless energy transfer systems, further referred to by the abbreviation CET, have been established in many technical applications [1], [2]. For low power applications, such as charging of consumer electronics, industrial standards as the Qi by the Wireless Power Consortium are already set [3]. For high power applications, such as wireless charging of electric vehicles, CET is an important object of research [4]–[10].

In this contribution, the design layout of near field CET-systems is divided into the setup of the coil system or coil arrangement, the reactive power compensation and the layout of inverter and rectifier. Different reactive power compensations lead to different system behaviors. The result is a varying response characteristic, which is represented with input impedance and transfer functions over the load resistance. Fig. 1 shows an overview of a CET-system.

The paper contributes to the system design for setups with known or otherwise computable magnetic parameters with a coil arrangement of two coils. In this case, it exists one primary side and one secondary side each with one coil and one compensation capacitor. Nonetheless, the calculations that are performed in this paper may be used for systems with more than two coils as well. By definition, the power transfer is defined from the primary side to the secondary side. To describe the system design itself, each subsystem in Fig. 1 is analyzed in the following three sections. The description starts with the magnetic parameters of the coil system and different compensation topologies and end with outlining the behavior of different rectifiers and inverters relating to the compensations. Finally, a comparison of two differently compensated systems regarding their calculations is presented.

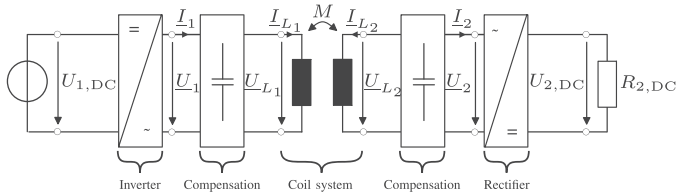

Fig. 1. Overview of a CET-system with used nomenclature.

Starting point for further calculations is the tuning of the primary and the secondary side to the same design frequency ω_d [11]. This design decision leads to a limited amount of topologies for reactive power compensations, each with its own specific system characteristic. The further explained design methods enable the identification of the reactive power compensation topology, which meets the requirements best.

For known magnetic parameters, which are the coupling factor k as well as the magnetic permeances Λ_1 and Λ_2, the equations describing the transfer functions allow to define the optimal number of turns for the windings of the inductances L_1 and L_2. In the ideal case, the resulting load dependent voltage transfer function is then likely to fulfill the requirements without additional control systems.

II. Coil System

The overall system design itself relies on the magnetic parameters of the respective coil system. Different coil geometries and arrangements are possible depending on the use case, which is shown by a comparison in [12] and [13]. An alternating current in the primary coil leads to an alternating magnetic field. To increase the efficiency in practical implementations, the alternating current should have a frequency higher than 20 kHz [14].

Manuscript received September 12, 2017; revised January 29, 2018; accepted March 2, 2018. Date of publication August 19, 2018; date of current version December 12, 2018. Paper 2017-EMC-1051.R1 presented at the 2016 IEEE International Power Electronics and Motion Control Conference, Varna, Bulgaria, Sep. 25–28, and approved for publication in the IEEE Transactions on Industry Applications by the Electric Machines Committee of the IEEE Industry Applications Society. *(Corresponding author: David Maier.)*

The authors are with the Institute of Electrical Energy Conversion, University of Stuttgart, Stuttgart 70569, Germany (e-mail: david.maier@iew.uni-stuttgart.de; joerg.heinrich@iew.uni-stuttgart.de; marco.zimmer@iew.uni-stuttgart.de; marcel.maier@iew.uni-stuttgart.de; parspour@iew.uni-stuttgart.de).

Color versions of one or more of the figures in this paper are available online at http://ieeexplore.ieee.org.

Digital Object Identifier 10.1109/TIA.2018.2866247

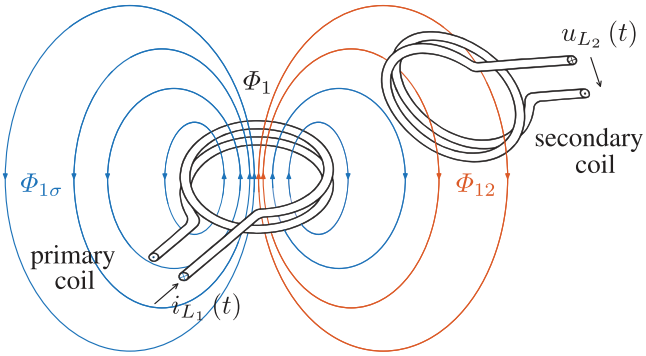

Fig. 2. Magnetic flux visualization of the primary coil with opened secondary coil; Stray magnetic flux $\Phi_{1\sigma}$ in blue and main magnetic flux $\Phi_{\mathrm{h}} = \Phi_{12} + \Phi_{21}$ in red; $\Phi_{21} = 0$, since the secondary coil is opened.

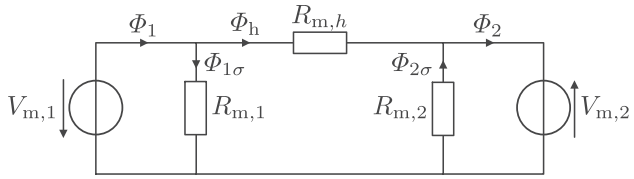

Fig. 3. Magnetic equivalent circuit for a coil system with two coils.

According to Fig. 2, the resulting magnetic flux Φ_1 is separated into the main flux Φ_{12} and the stray magnetic flux $\Phi_{1\sigma}$.

By taking the secondary coil into account, another magnetic flux Φ_2 occurs based on the magnetic field of the primary side. The resulting interaction of both coils is represented with

$$\Phi_1(t) = \Phi_{1\sigma}(t) + \underbrace{\Phi_{12}(t) + \Phi_{21}(t)}_{\Phi_{\mathrm{h}}} \tag{1}$$

and

$$\Phi_2(t) = \Phi_{2\sigma}(t) + \underbrace{\Phi_{21}(t) + \Phi_{12}(t)}_{\Phi_{\mathrm{h}}}. \tag{2}$$

To model the coil system, it is useful to represent the flux in a magnetic equivalent circuit as shown in Fig. 3. The magnetic properties of the coil's surrounding volume are represented with magnetic resistances. For a two-coil system, there are three magnetic resistances.

The ratio between the single magnetic fluxes and the magnetic resistances lead to the key magnetic parameters of an actual coil arrangement. These are the coupling factor k and the permeance of both windings Λ_1 and Λ_2 [15]. For the analytic calculation, there are several possibilities to model the system.

One way is based on the magnetic equivalent circuit by the use of a gyrator capacitor model as it is described in [16], which is useful for coil systems with more than two coils. Another way is to use the elements in the magnetic equivalent circuit together with the law of induction that lead to

$$\begin{pmatrix} \underline{U}_{L_1} \\ \underline{U}_{L_2} \end{pmatrix} = \begin{pmatrix} L_1 & k \cdot \sqrt{L_1 L_2} \\ k \cdot \sqrt{L_1 L_2} & L_2 \end{pmatrix} \cdot \begin{pmatrix} \underline{I}_{L_1} \\ \underline{I}_{L_2} \end{pmatrix} \tag{3}$$

if losses are neglected. Equation (3) describes the well known transformer equivalent circuit with respect to the used nomenclature presented in Fig. 1. Contactless inductive energy transfer systems have, in contrary, a small magnetic coupling factor k. In this case, it is useful to describe the two-coil system with a two-port network as it is shown in Fig. 4.

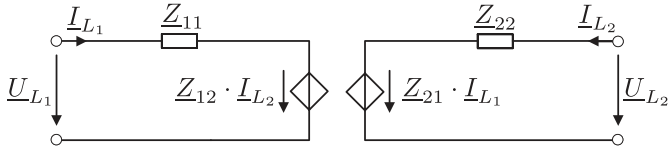

Fig. 4. Equivalent circuit for a two-coil system represented as a two-port network with $\underline{Z}$-parameters.

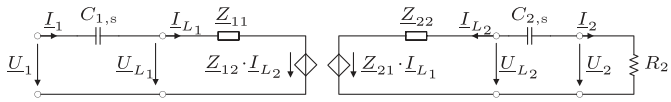

Fig. 5. Equivalent circuit of a 1s2s-compensated system with $\underline{Z}$-parameters.

Deriving (3) partially, with respect to the current, leads to the impedance matrix $\underline{Z}$, which defines the elements in Fig. 4

$$\underline{Z} = \begin{pmatrix} \underline{Z}_{11} & \underline{Z}_{12} \\ \underline{Z}_{21} & \underline{Z}_{22} \end{pmatrix} = \begin{pmatrix} \left.\frac{\partial \underline{U}_{L_1}}{\partial \underline{I}_{L_1}}\right|_{\underline{I}_{L_2}=0} & \left.\frac{\partial \underline{U}_{L_1}}{\partial \underline{I}_{L_2}}\right|_{\underline{I}_{L_1}=0} \\ \left.\frac{\partial \underline{U}_{L_2}}{\partial \underline{I}_{L_1}}\right|_{\underline{I}_{L_2}=0} & \left.\frac{\partial \underline{U}_{L_2}}{\partial \underline{I}_{L_2}}\right|_{\underline{I}_{L_1}=0} \end{pmatrix}. \tag{4}$$

A part from modeling the coil arrangement with the impedance parameters, it is also possible to use the admittance, hybrid, or inverse hybrid parameters. Depending on the use case, each method can facilitate further calculations.

III. Topologies of CET-Systems

Generally, there are four different combinations to compensate a CET-system with one capacitor at each side. Every combination of serial (s) or parallel (p) compensation on primary (1) and secondary (2) side is possible. Besides, there are other compensation topologies with more than one capacitor or inductor at each side.

A. Behavior of a 1s2s-System

For the analytical computation of a serially compensated system on both sides, further referred to by the abbreviation 1s2s, $\underline{Z}$-parameters provide the most convenient calculation method. Therefore, the coil arrangement is defined as a two-port network compared to Fig. 4. Solving (4), for this case, leads to

$$\begin{aligned} \underline{Z}_{11} &= \mathrm{j}\omega L_1 & \underline{Z}_{12} &= \mathrm{j}\omega M \\ \underline{Z}_{21} &= \mathrm{j}\omega M & \underline{Z}_{22} &= \mathrm{j}\omega L_2. \end{aligned} \tag{5}$$

With this approach, it is possible to do further calculations considering the reactive power compensation for a both side serially compensated system, which is also shown in Fig. 5.

By using Kirchhoff's laws, the left- and the right-hand side of Fig. 5 yields to

$$\underline{U}_{L_2} = \underline{Z}_{21}\underline{I}_{L_1} + \underline{Z}_{22}\underline{I}_{L_2} = -\underline{I}_{L_2}\left(\frac{1}{\mathrm{j}\omega \mathrm{C}_{2,\mathrm{s}}} + R_2\right)$$

$$\Rightarrow \underline{I}_{L_2} = -\underline{I}_{L_1}\frac{\underline{Z}_{21}}{\underline{Z}_{22} + \frac{1}{\mathrm{j}\omega \mathrm{C}_{2,\mathrm{s}}} + R_2}$$

$$\underline{U}_1 = \underline{I}_1\left(\frac{1}{\mathrm{j}\omega \mathrm{C}_{1,\mathrm{s}}} + \underline{Z}_{11}\right) + \underline{Z}_{12}\underline{I}_{L_2}. \tag{6}$$

Inserting the $\underline{Z}$-parameters from (5), the mutual inductance $M = k\sqrt{L_1 L_2}$ and $\underline{I}_1 = \underline{I}_{L_1}$, (6) is solved for the input impedance $\underline{Z}_{\mathrm{IN}}$ to

$$\underline{Z}_{\mathrm{IN}} = \underbrace{\frac{1}{\mathrm{j}\omega \mathrm{C}_{1,\mathrm{s}}} + \mathrm{j}\omega L_1}_{\stackrel{!}{=}\mathrm{j}X_1} + \underbrace{\frac{\omega^2 k^2 L_1 L_2}{\mathrm{j}\omega L_2 + \frac{1}{\mathrm{j}\omega \mathrm{C}_{2,\mathrm{s}}} + R_2}}_{\stackrel{!}{=}\mathrm{j}X_2}. \tag{7}$$

Given that the primary and the secondary side are tuned to the same design frequency ω_d, the values of the compensation capacitors are defined by

$$C_{1,\mathrm{s}} = \frac{1}{\omega_\mathrm{d}^2 L_1} \quad \text{and} \quad C_{2,\mathrm{s}} = \frac{1}{\omega_\mathrm{d}^2 L_2}. \tag{8}$$

Inserting (8) in (7), the reactances X_1 and X_2 are expressed as

$$X_1 = \omega L_1\left(1 - \frac{{\omega_\mathrm{d}}^2}{\omega^2}\right) \quad \text{and} \quad X_2 = \omega L_2\left(1 - \frac{{\omega_\mathrm{d}}^2}{\omega^2}\right). \tag{9}$$

Through substituting X_1 and X_2 in (7) with (9), the input impedance simplifies to

$$\underline{Z}_{\mathrm{IN}} = \frac{\omega^2 k^2 L_1 L_2 R_2}{X_2^2 + R_2^2} + \mathrm{j}\underbrace{\left[X_1 - X_2\frac{\omega^2 k^2 L_1 L_2}{X_2^2 + R_2^2}\right]}_{\stackrel{!}{=}X_{\mathrm{IN}}}. \tag{10}$$

The approach described here is limited to resonant systems. These systems have e.g., a better efficiency through lower switching losses and for that reason high practical relevance. Therefore, the reactance X_{IN} has to tend to zero. Due to the system's dimensioning with ω_d, two cases are distinguished.The first one is $X_1 = X_2 = 0$, which leads to

$$\omega_{\mathrm{r}0} = \omega_\mathrm{d}. \tag{11}$$

The second one comprises $X_2 \neq 0$, which implies that X_1 is also nonzero, because both terms depend on ω_d. Resolving $X_{\mathrm{IN}} = 0$ with respect to this condition leads to two additional solutions

$$\omega_{\mathrm{r}1,\mathrm{r}2} = \frac{\omega_\mathrm{d}}{\sqrt{1 - \frac{R_2^2}{2{\omega_\mathrm{d}}^2 L_2^2} \pm \sqrt{\left(1 - \frac{R_2^2}{2{\omega_\mathrm{d}}^2 L_2^2}\right)^2 - (1-k^2)}}}. \tag{12}$$

These solutions exist for a discriminant greater or equal to zero, which implies that $\omega_{\mathrm{r}1,\mathrm{r}2}$ is only defined for

$$R_2 \leq \underbrace{\omega_\mathrm{d} L_2\sqrt{2 - 2\sqrt{1-k^2}}}_{\stackrel{!}{=}R_{2,\mathrm{c}}}. \tag{13}$$

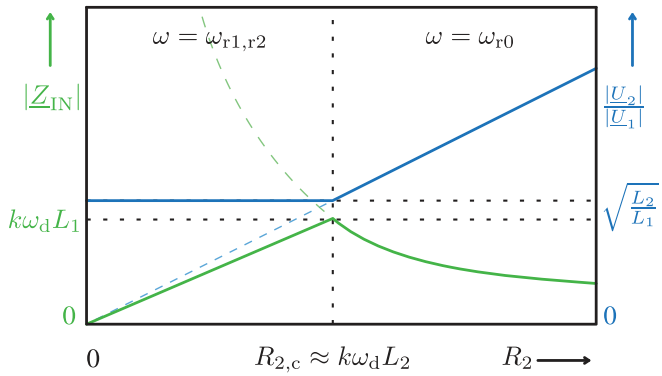

Fig. 6. Transfer function and input impedance of a 1s2s-system [17].

The relevant equivalent load resistance, separating the resonant frequencies, is further called the characteristic resistance $R_{2,\mathrm{c}}$. For coupling factors close to zero, the limit of (13) is expressed with a PUISEUX series at $k = 0$ to

$$\lim_{k\to 0} R_{2,\mathrm{c}} = k\omega_\mathrm{d}L_2 + \frac{1}{8}k^3\omega_\mathrm{d}L_2 + \frac{7}{128}k^5\omega_\mathrm{d}L_2 + \cdots \tag{14}$$

On the basis of this, the characteristic resistance is simplified to

$$R_{2,\mathrm{c}} \approx k\omega_\mathrm{d}L_2 \tag{15}$$

for coupling factors up to $k = 0.5$. Then, all other terms of the series rapidly tend to zero. For $k = 0.5$, the inaccuracy is approximately 3.41%.

With this knowledge, the input impedance $\underline{Z}_{\mathrm{IN}}$ and the voltage transfer function $M_\mathrm{U} = \frac{|\underline{U}_2|}{|\underline{U}_1|}$ are calculated for the resonant frequencies. This leads to

$$|\underline{Z}_{\mathrm{IN}}| = \frac{{\omega_{\mathrm{r}0}}^2 k^2 L_1 L_2}{R_2} \qquad M_\mathrm{U} = \frac{R_2}{\omega_{\mathrm{r}0} k\sqrt{L_1 L_2}} \tag{16}$$

for $\omega_{\mathrm{r}0}$ and

$$|\underline{Z}_{\mathrm{IN}}| = R_2\frac{L_1}{L_2} \qquad M_\mathrm{U} = \sqrt{\frac{L_2}{L_1}} \tag{17}$$

for $\omega_{\mathrm{r}1,\mathrm{r}2}$.

Fig. 6 shows the behavior in resonant operation with the resonant frequencies $\omega_{\mathrm{r}0}$ or $\omega_{\mathrm{r}1,\mathrm{r}2}$ for $R_2 \leq R_{2,\mathrm{c}}$ and $\omega_{\mathrm{r}0}$ for $R_2 > R_{2,\mathrm{c}}$.

In addition, the transimpedance function $M_\mathrm{Z} = \frac{|\underline{U}_2|}{|\underline{I}_1|}$, the transadmittance function $M_\mathrm{Y} = \frac{|\underline{I}_2|}{|\underline{U}_1|}$, and the current transfer function $M_\mathrm{I} = \frac{|\underline{I}_2|}{|\underline{I}_1|}$ are obtained by

$$M_\mathrm{Z} = M_\mathrm{U}\cdot|\underline{Z}_{\mathrm{IN}}| \qquad M_\mathrm{Y} = \frac{M_\mathrm{U}}{R_2} \qquad M_\mathrm{I} = \frac{M_\mathrm{Z}}{R_2}. \tag{18}$$

B. Behavior of a 1s2p-System

A primary side serially and secondary side parallel compensated coil arrangement is calculated identically to the 1s2s-system. A detailed analytical calculation was done in [17]. Hence, only the response characteristic of a 1s2p-system is

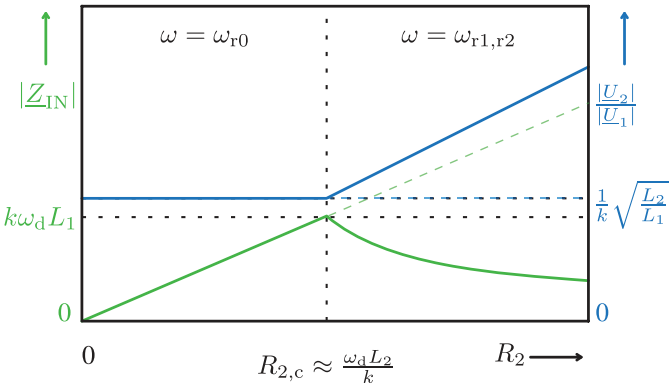

Fig. 7. Transfer function and input impedance of a 1s2p-system [17].

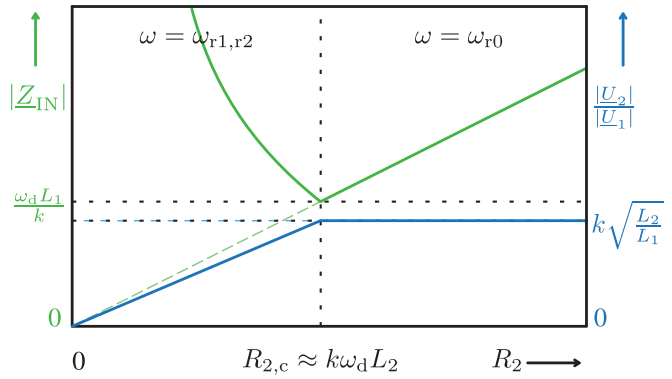

Fig. 8. Transfer function and input impedance of a 1p2s-system [17].

presented for the three resonant frequencies with

$$|\underline{Z}_{IN}| = R_2 k^2 \frac{L_1}{L_2} \qquad M_U = \frac{1}{k}\sqrt{\frac{L_2}{L_1}} \tag{19}$$

for ω_{r0} and

$$|\underline{Z}_{IN}| = \frac{{\omega_d}^2 L_1 L_2 \left(1-k^2\right)}{R_2} \qquad M_U = \frac{R_2}{\omega_d \sqrt{L_1 L_2 \left(1-k^2\right)}} \tag{20}$$

for $\omega_{r1,r2}$, which is represented in Fig. 7.

C. Behavior of a 1p2s-System

According to [17], the response characteristic of the primary side parallel and secondary side serially compensated system is described by

$$|\underline{Z}_{IN}| = \frac{R_2 L_1}{L_2 k^2} \qquad M_U = k\sqrt{\frac{L_2}{L_1}} \tag{21}$$

for ω_{r0} and

$$|\underline{Z}_{IN}| = \frac{{\omega_d}^2 L_1 L_2 \left(1-k^2\right)}{R_2} \qquad M_U = \frac{R_2}{\omega_d \sqrt{L_1 L_2 \left(1-k^2\right)}} \tag{22}$$

for $\omega_{r1,r2}$, which are plotted in Fig. 8.

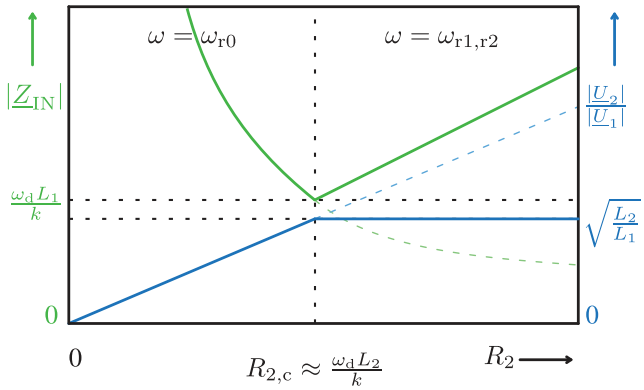

Fig. 9. Transfer function and input impedance of a 1p2p-system [17].

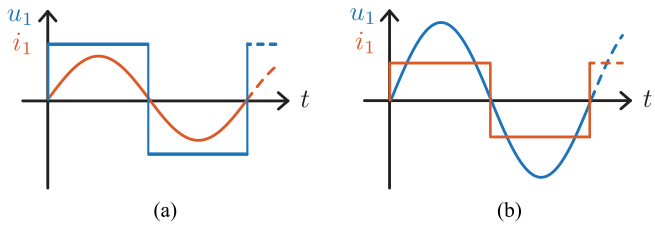

Fig. 10. Simplified voltage and current characteristic in (a) serial and (b) parallel compensated systems.

D. Behavior of a 1p2p-System

Likewise, the response characteristic of the primary side parallel and secondary side parallel compensated system is described by

$$|\underline{Z}_{IN}| = \frac{{\omega_{r0}}^2 L_1 L_2 \left(1-k^2\right)^2}{R_2 k^2} \qquad M_U = \frac{R_2 k}{\omega_{r0}\sqrt{L_1 L_2}\left(1-k^2\right)} \tag{23}$$

for ω_{r0} and

$$|\underline{Z}_{IN}| = R_2 \frac{L_1}{L_2} \qquad M_U = \sqrt{\frac{L_2}{L_1}} \tag{24}$$

for $\omega_{r1,r2}$ [17]. This behavior is shown in Fig. 9.

IV. Rectifier and Inverter

An essential part for the overall system is the primary side inverter and the secondary side rectifier. Considering the mains side of a CET-system, there are several other modules before the inverter, e.g., a power factor correction and a mains line filter. These parts are not considered in this paper, why it is assumed that a intermediate circuit with a constant voltage source exists on the primary side. Depending on the reactive power compensation, the system's rectifier or inverter is build up and operated differently. In contrast to the voltage source for serial compensation, a current source is needed for a parallel compensation. Fig. 10 shows the mentioned current and voltage characteristics without harmonics behind the inverter.

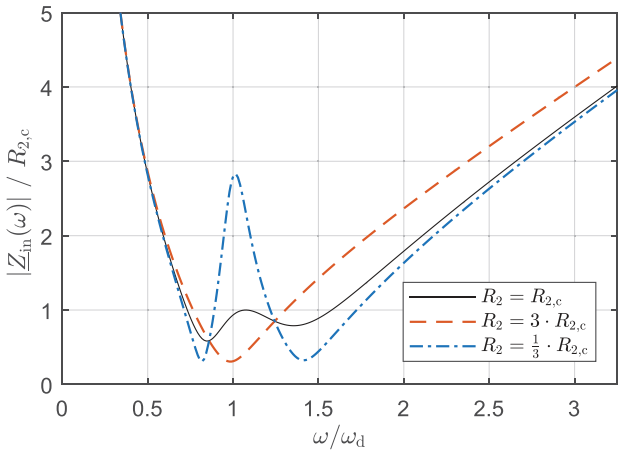

Fig. 11. Ratio of input impedance to characteristic resistance over the normalized frequency for three different load resistances R_2 and coupling factor $k = 0.5$.

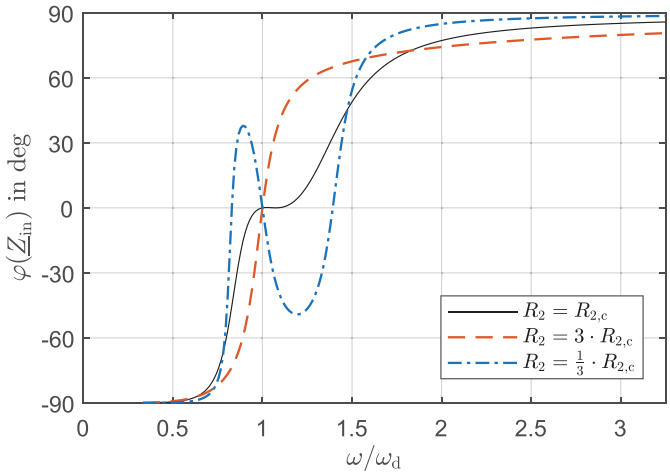

Fig. 12. Phase of input impedance $\underline{Z}_{\mathrm{IN}}$ over the normalized frequency for three different load resistances R_2 and coupling factor $k = 0.5$.

A. Neglecting Harmonics as a Useful Approximation

CET-systems with a reactive power compensation on both sides act as a harmonic filter, which is damping all harmonics under most conditions. A combination of block-shaped input voltage $u_1(t)$ and a primary-side serial compensation (1s) leads to a filter which suppresses harmonics in the input current $i_1(t)$. In the same way, the input voltage harmonics are suppressed by the combination of a block-shaped input current and a parallel compensation (1p). Fig. 10 presents the mentioned behavior without the consideration of harmonics.

The following statements, based on calculations and simulations, are valid for CET-systems with a reactive power compensation as per Section III and a coupling factor $k < 0.5$.

1) The harmonics' amplitudes are moderately high at under 15% compared to the fundamental, if the load resistance R_2 deviates not to much from the characteristic resistance $R_{2,\mathrm{c}}$. Based on a 1s2s-system, the specific values for $|\underline{Z}_{\mathrm{IN}}|(\omega)$ over $R_{2,\mathrm{c}}$ are presented in Fig. 11, which shows the mentioned behavior in general.
2) The influence of the harmonics on the transferred power is insignificantly small. This is shown by (26) with a consideration of the third-harmonic phase angle.
3) Linking the last both statements entails that considering only the fundamental of the rectangular input voltage or current is an admissible approach. Hence, the calculations in Section III allow a design procedure with the inclusion of rectifier and inverter at early design stages.

Exemplary for a 1s2s-topology, the insignificantly small influence of the third harmonic current amplitude $\hat{i}_{1,\mathrm{k3}}$ on the transferred power P_{l} is calculated in (26) based on

$$\hat{i}_{1,\mathrm{k3}}(t) = \frac{\hat{u}_{1,\mathrm{k3}}(t)}{|\underline{Z}_{\mathrm{IN}}(3\omega_{\mathrm{d}})|} \cdot \sin\left(3\omega_{\mathrm{d}}t - \varphi_{(\underline{Z}_{\mathrm{IN}}(3\omega_{\mathrm{d}}))}\right)$$

$$i_{1,\mathrm{k3}}(t) \approx \hat{i}_{1,\mathrm{k3}} \cdot -\cos(3\omega_{\mathrm{d}}t) \text{ with } \varphi_{(\underline{Z}_{\mathrm{IN}}(3\omega_{\mathrm{d}}))} \approx \frac{\pi}{2}. \quad (25)$$

In (25), the phase angle of the third harmonic is rounded to $\varphi = 90°$ for simplification. The validity of this approximation is apparent from Fig. 12, which shows the phase angle for different load resistances with respect to the normalized frequency. It becomes obvious that the phase angle of $\underline{Z}_{\mathrm{IN}}(3\omega_{\mathrm{d}})$ or $\underline{Z}_{\mathrm{IN}}(1/3 \cdot \omega_{\mathrm{d}})$ is between 80° and 89°, why it is neglected in (25)

$$P_{\mathrm{l}}(\omega_{\mathrm{d}}) \approx \frac{2 \cdot U_{1,\mathrm{DC}}}{T} \cdot \int_0^{T/2} \left(\hat{i}_{1,\mathrm{k1}} \sin(\omega_{\mathrm{d}}t) - \hat{i}_{1,\mathrm{k3}} \cos(3\omega_{\mathrm{d}}t)\right) \mathrm{d}t$$

$$P_{\mathrm{l}}(\omega_{\mathrm{d}}) \approx \underbrace{\frac{2 \cdot U_{1,\mathrm{DC}}}{T}}_{2 \cdot f_{\mathrm{d}} \cdot U_{1,\mathrm{DC}}} \cdot \left(\underbrace{\left[\frac{-\hat{i}_{1,\mathrm{k1}} \cos(\omega_{\mathrm{d}}t)}{\omega_{\mathrm{d}}}\right]_0^{T/2}}_{\frac{2\cdot\hat{i}_{1,\mathrm{k1}}}{\omega_{\mathrm{d}}} = \frac{2\cdot\hat{i}_{1,\mathrm{k1}}}{2\cdot\pi\cdot f_{\mathrm{d}}}} + \underbrace{\left[\frac{\hat{i}_{1,\mathrm{k1}} \sin(3\omega_{\mathrm{d}}t)}{3\omega_{\mathrm{d}}}\right]_0^{T/2}}_{0} \right)$$

$$P_{\mathrm{l}}(\omega_{\mathrm{d}}) \approx \frac{2 \cdot \sqrt{2}}{\pi} \cdot U_{1,\mathrm{DC}} \cdot I_{1,\mathrm{k1}} \approx 0.90 \cdot U_{1,\mathrm{DC}} \cdot I_{1,\mathrm{k1}} \quad (26)$$

$$P_{\mathrm{l}}(\omega_{\mathrm{d}}) \approx \left(\frac{2 \cdot \sqrt{2}}{\pi}\right)^2 \cdot \frac{U_{1,\mathrm{DC}}^2}{|\underline{Z}_{\mathrm{IN}}(\omega_{\mathrm{d}})|} \approx 0.81 \cdot \frac{U_{1,\mathrm{DC}}^2}{|\underline{Z}_{\mathrm{IN}}(\omega_{\mathrm{d}})|}. \quad (27)$$

As expected, the result in (26) corresponds to the factor $^4/_{\pi}$ for the fundamental of the fourier series of a rectangular voltage with $\pm U_{1,\mathrm{DC}}$, in this case $\hat{u}_{1,\mathrm{k1}} = {}^4/_{\pi} \cdot U_{1,\mathrm{DC}}$. This consideration for the third-order harmonic is representative for all higher order harmonics, since the influence on the transferred power P_{l} decreases even more with higher order harmonics. Similarly, the calculations for $k = 0.5$ cover the worst-case scenario, since the effect on the transferred power increases likewise with decreasing coupling factor.

TABLE I
CONVERSION FACTORS FOR EQUIVALENT SINUSOIDAL INPUT VOLTAGES

inverter-type	primary-side topology	equivalent input voltage
voltage DC-link	serial (1s)	$U_1 = \frac{2\cdot\sqrt{2}}{\pi} \cdot U_{1,\mathrm{DC}}$
current DC-link	parallel (1p)	$U_1 = \frac{\pi}{2\cdot\sqrt{2}} \cdot U_{1,\mathrm{DC}}$

TABLE II
CONVERSION FACTORS FOR SECONDARY SIDE DC-LINK VOLTAGES

rectifier-type	secondary-side topology	equivalent DC-link voltage
voltage DC-link	serial (2s)	$U_{2,\mathrm{DC}} = \frac{\pi}{2\cdot\sqrt{2}} \cdot U_2$
current DC-link	parallel (2p)	$U_{2,\mathrm{DC}} = \frac{2\cdot\sqrt{2}}{\pi} \cdot U_2$

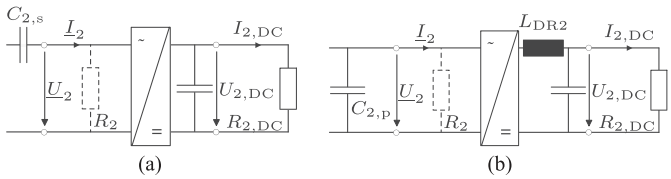

Fig. 13. Rectifier with a resistor for secondary (a) serially and (b) parallel compensated system.

B. Load Resistance and Voltage Conversion Factors

Based on last equations, conversion factors are found. The factors are listed in Table I and they determine the value for the equivalent sinusoidal input voltage U_1.

Applying the same relationships between the average value of the block shaped voltage or current and the equivalent sinusoidal, leads to the conversion factors for the rectifiers listed in Table II.

Different secondary side voltages lead to different equivalent load resistances. This influence has to be considered in the system design process. Additionally, the secondary side DC-link load resistance $R_{2,\mathrm{DC}}$ and the secondary side AC equivalent resistance R_2 are presented with the notation of current and voltage values for both resistances in Fig. 13.

If losses and harmonics are neglected, the available output power P_2 is constant regardless of the use of a rectifier with zero degree commutation angle

$$P_2 = U_2 \cdot I_2 = U_{2,\mathrm{DC}} \cdot I_{2,\mathrm{DC}}$$

$$P_2 = \frac{U_2^2}{R_2} = \frac{U_{2,\mathrm{DC}}^2}{R_{2,\mathrm{DC}}}. \tag{28}$$

The conversion factors in Table III are compatible to (28) and match the DC-link load resistance $R_{2,\mathrm{DC}}$ to the AC equivalent load resistance R_2.

To design a system with a fixed maximum output power $P_{\max}$ and a constant secondary side DC-link voltage $U_{2,\mathrm{DC}}$, the DC-link load resistance should match the assigned maximum power calculated with $R_{2,\mathrm{DC}}(P_{\max}) = {U_{2,\mathrm{DC}}^2}/{P_{\max}}$. With the conversion factors of Table III, the equivalent load resistance $R_2(P_{\max})$ is obtained, which is used for further calculations. The system design is discussed in detail in Section V-B.

TABLE III
CONVERSION FACTORS FOR SECONDARY SIDE DC-LINK VOLTAGES

rectifier-type	secondary-side topology	equivalent load resistance
voltage DC-link	serial (2s)	$R_2 = \left(\frac{2\cdot\sqrt{2}}{\pi}\right)^2 \cdot R_{2,\mathrm{DC}}$
current DC-link	parallel (2p)	$R_2 = \left(\frac{\pi}{2\cdot\sqrt{2}}\right)^2 \cdot R_{2,\mathrm{DC}}$

V. EXPERIMENTAL SETUP AND DESIGN PROCEDURE

The knowledge about different transfer functions as well as the influence of inverter and rectifier allows an expedient and structured design procedure for various CET-systems. The procedure requires the knowledge of the coil arrangement's magnetic parameters and the system's technical constraints like voltage level or output power. Furthermore, the system boundaries, e.g., the maximum tolerable frequency, have to be taken into account to ensure a high efficiency and robustness. Typically, the desired frequency is selected such that the quality factor Q of the coil arrangement reaches its maximum. In general, a higher quality factor Q of the coil arrangement leads to a better efficiency [3]. The fundamental design process is described in [17], whereas in this paper a comparison of two different compensation topologies with an identical coil system is presented. For the coil system, two solenoid coils are used. As the measurement in Section V-B shows, the quality factor of solenoid coils is comparatively high, which leads to very good measurement results.

A. Finite Element Simulation

Prior to the designing process, the magnetic parameters and the coil arrangement should be well known. Therefore, a numerical three dimensional (3D) – finite element simulation (FEM) simulation is done and presented in Fig. 14.

The 3D-FEM model consists of two identical solenoid coils with flux guidance. The winding space of the solenoid coil amounts to 2 mm in height and 25 mm in width. It is wound around the four ferrite rods in the middle. Each rod amounts to 15 mm by 3 mm by 110 mm. To determine the magnetic coupling factor, the model is simulated twice, first, with an opened secondary coil to calculate the value of the inductance L_1, and second with a short-circuited secondary side coil to calculate the influence on the primary side inductance $L_{1,\mathrm{s}}$. Based on (3) and a shorted transformer equivalent circuit, the magnetic coupling is calculated to

$$k = \sqrt{1 - \frac{L_{1,\mathrm{s}}}{L_1}}. \tag{29}$$

The entire coil system is described with the coupling factor and the magnetic conductance. The parameters gained by the FEM simulation are shown in Table IV.

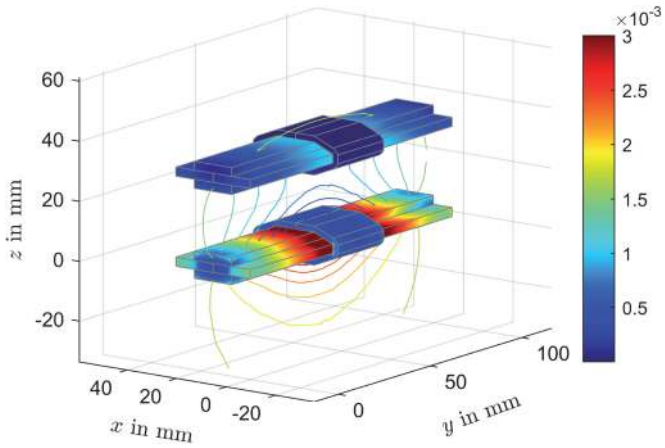

Fig. 14. Simulated coil system with a current of 1 A in the primary coil and a shorted secondary coil to calculate the coupling factor k; the color bar shows the magnetic flux density as a surface plot and the contour lines refer to the magnetic vector potential.

TABLE IV
KNOWN CHARACTERISTICS

Parameter		Value
Magnetic permeance	Λ_1	160 nH
Magnetic permeance	Λ_2	160 nH
Design coupling factor	k_d	0.27

These parameters are valid for different number of turns as long as the coil windings are homogeneously distributed in the modeled area.

B. System Design

In this section, two systems with two different compensation topologies of Section III are designed. In the first case, a 1p2p-system for a constant voltage power supply is designed. In the second case, a charging unit for a battery system is build up using a 1s2s-system.

For the contactless constant-voltage power supply, it is advisable to select the operation point at the resonant frequency $\omega_{\mathrm{r}1,\mathrm{r}2}$. This guarantees a constant output voltage for all operating cases, from idle at $R_{2,\mathrm{DC}} \to \infty$ to the maximum transferred power, with the load resistance equal to the characteristic resistance $R_{2,\mathrm{DC,c}}$.

In contrast, a variable voltage is advisable for a battery charging system. Therefore, the operating point for the 1s2s-system is set to the resonant frequency $\omega_{\mathrm{r}0}$. As presented in Fig. 6 the battery voltage can attain arbitrary values for $\omega = \omega_{\mathrm{r}0}$, whereas for $\omega = \omega_{\mathrm{r}1,\mathrm{r}2}$, only a fixed voltage is possible. Furthermore, the battery is charged in constant current mode which is calculated with (18), if solved for I_2.

In both cases, the maximum efficiency of the coil system and the reactive power compensation varies depending on the operating point. Neglecting the influence of inverter and rectifier, the maximum efficiency is gained at the characteristic resistance $R_{2,\mathrm{c}}$ [18].

TABLE V
DESIRED CHARACTERISTICS

Parameter	Value
Input voltage $U_{1,\mathrm{DC}}$	24 V
Output voltage $U_{2,\mathrm{DC}}$	24 V
Nominal output Power P_2	50 W
Design frequency f_d	150 kHz

For the 1p2p- and 1s2s-system, different power electronics are needed. In case of the parallel compensated system, the appropriate choice of power electronics is an auto-resonant royer oscillator described in [19]–[21] for the primary side and an active center-tap full wave rectifier on the secondary side. As parallel compensated systems require a current source, a choke is used in the royer oscillator as well as in the rectifier for this purpose. The oscillator is operated with constant voltage and allows a conversion to an alternating voltage without any further control systems.

In case of the serially compensated system, a single phase DC–AC full bridge inverter with MOSFETs and full bridge passive rectifier with silicon carbide Schottky diodes is used.

According to Section IV and the selected power electronics, the input voltage and the load resistance is calculated to

$$U_1 = \frac{\pi}{\sqrt{2}} \cdot U_{1,\mathrm{DC}} \qquad R_2 = \frac{\pi^2}{2} \cdot R_{2,\mathrm{DC}} \tag{30}$$

for the 1p2p-system [11] and to

$$U_1 = \frac{2 \cdot \sqrt{2}}{\pi} \cdot U_{1,\mathrm{DC}} \qquad R_2 = \frac{8}{\pi^2} \cdot R_{2,\mathrm{DC}} \tag{31}$$

for the 1s2s-system.

For a high efficiency, the desired frequency should be determined by the highest value of the quality factor Q, if both coil systems are identical. In this setup, Q has its maximum at a frequency of roughly 150 kHz. Therefore, the design frequency ω_d is set to 150 kHz. At this frequency, Q amounts to 550. The measurements are done with a HIOKI IM 3532 LCR meter. To compare both the systems, identical system characteristics are assumed. The defined system requirements are presented in Table V.

With the desired and known characteristics, the values of capacitors and inductances are calculated. As aforementioned, the maximum system efficiency is reached by a load resistance near the characteristic resistance. Including this fact, the desired value of the characteristic resistance is calculated with

$$R_2 = \frac{U_2^2}{P_2} \ . \tag{32}$$

To consider losses and tolerances, the output power P_2 is set to different values depending on the used topology. For a 1p2p-system, the maximum output power is gained at the characteristic resistance $R_{2,\mathrm{c}}$ as it is calculated with the equations of Section III-D. For a 1s2s-system, the minimum output power is gained at the characteristic resistance $R_{2,\mathrm{c}}$ as it is calculated with the equations of Section III-A. Since the operating point is set near the characteristic resistance, this circumstances lead

TABLE VI
MEASURED DATA OF THE SYSTEM

Measurand	Values 1p2p-system	Values 1s2s-system
L_1	11.30 µH	45.51 µH
L_1	11.25 µH	45.88 µH
k	0.2559	0.2706
C_1	94.60 nF	24.01 nF
C_2	94.25 nF	23.96 nF

to different assumed output powers for the calculation. For the 1p2p-system, the output power is set to a higher value of about 75 W, whereas for the 1s2s-system to a lower value of about 40 W. The values arise from estimated losses, component tolerances, and gained experience from different system designs.

The calculation results in $R_{2,\mathrm{c}} = 37,89\,\Omega$ for the 1p2p-system and in $R_{2,\mathrm{c}} = 11,67\,\Omega$ for the 1s2s-system. With the desired system design frequency and the designed coupling factor, the inductance L_2 is calculated with the characteristic resistance $R_{2,\mathrm{c}}$, presented in Fig. 9 to

$$L_2 = \frac{k_\mathrm{d} \cdot R_{2,\mathrm{c}}}{f_\mathrm{d} \cdot 2\pi} = 10.85\,\mu\mathrm{H} \tag{33}$$

for the 1p2p-system and on the contrary with (13) to

$$L_2 = \frac{R_{2,\mathrm{c}}}{k_\mathrm{d} \cdot f_\mathrm{d} \cdot 2\pi} = 45.87\,\mu\mathrm{H} \tag{34}$$

for the 1s2s-system. With the known magnetic parameters from Table IV, it is possible to calculate the winding numbers of L_1 and L_2 by

$$N_2 = \sqrt{\frac{L_2}{A_2}} \tag{35}$$

and

$$N_1 = N_2 \sqrt{\frac{A_2}{A_1}} \cdot \frac{U_1}{U_2}. \tag{36}$$

This equations are valid for both topologies, because (17) and (24) are identical. The solution leads to eight windings for the parallel system and 17 windings for the serial system, respectively. In a final step, the values of the capacitors are calculated with (8) to $C_{1,\mathrm{s}} = C_{2,\mathrm{s}} = 24\,\mathrm{nF}$ and identically to $C_{1,\mathrm{p}} = C_{2,\mathrm{p}} = 103.75\,\mathrm{nF}$ for the parallel compensated system.

After setting up the system, a measurement was done. The results are shown in Table VI.

It is recognizable that there are some differences between the calculated values and the measured ones, which slightly affects the design frequency. The experimental setup is presented in Fig. 15 without the active center-tap full wave rectifier.

VI. MEASUREMENT AND RESULTS

To confirm the derivated equations with measurements, the two systems described in Section V are put in operation.

A. 1p2p-Compensated System

Fig. 16 shows the measured voltage transfer function M_U and the system's resonant frequency f over the equivalent load resistance R_2. The measured value of $R_{2,\mathrm{c}}$ is approximately 42 Ω, which fits well to the calculated value based on the measured data of Table VI.

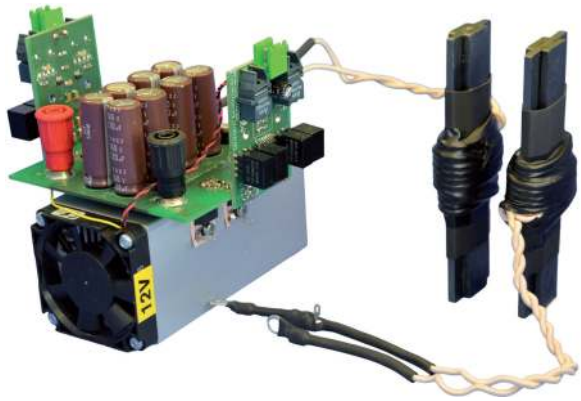

Fig. 15. Experimental setup – coil arrangement, compensation and inverter of primary side for the 1s2s-system; Dimensions: airgap ≈ 2 cm, length of ferrite rod 110 mm, length of heat sink 100 mm.

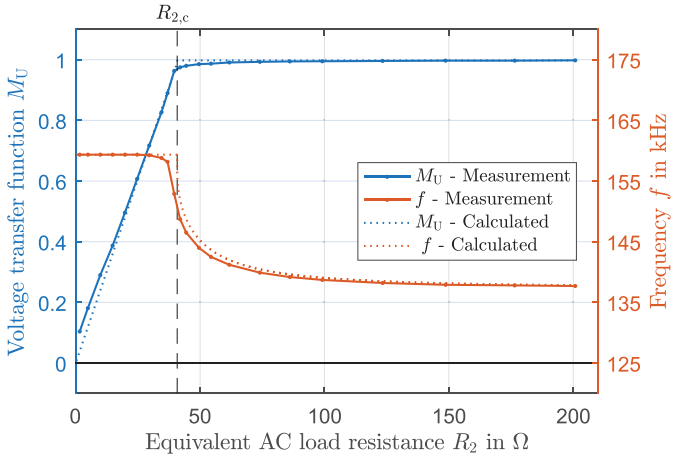

Fig. 16. Voltage transfer function and frequency of a 1p2p-system; calculated versus measured.

The calculated values M_U and f, gained with the equations of Section III-D for the different system resonant frequencies $\omega_{\mathrm{r}1,\mathrm{r}2}$ and $\omega_{\mathrm{r}0}$, are also plotted in the figure. Equally to Fig. 16, the calculated and measured values of the input impedance Z_IN and the output current I_2 are plotted with respect to the load resistance $R_{2,\mathrm{DC}}$ in Fig. 17.

Due to the center-tap rectifier, the load resistance is transformed as described in Table III in Section IV-B. Since the fundamentals of a center tap rectifier and a full bridge rectifier differ from each other, the equation to calculate the resistance deviates from the one in Table III. For the center tap rectifier the equation simplifies to

$$R_2 = \left(\frac{\pi}{\sqrt{2}}\right)^2 \cdot R_{2,\mathrm{DC}} \tag{37}$$

for the current DC-link 2p-system. Finally, the output power P_2 and the overall efficiency eta are shown in Fig. 18.

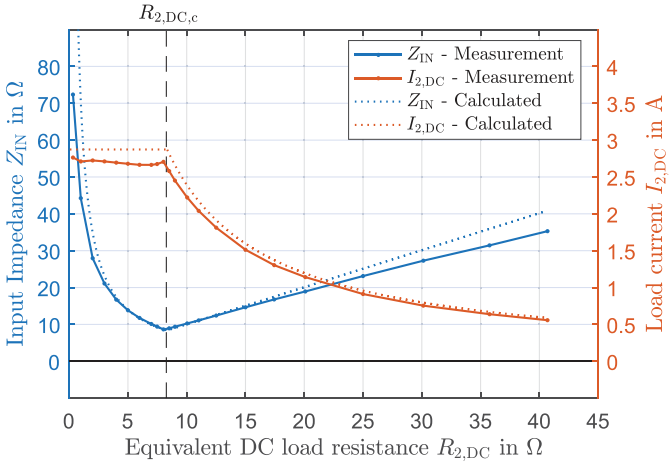

Fig. 17. Input impedance and output current of a 1p2p-system; calculated versus measured.

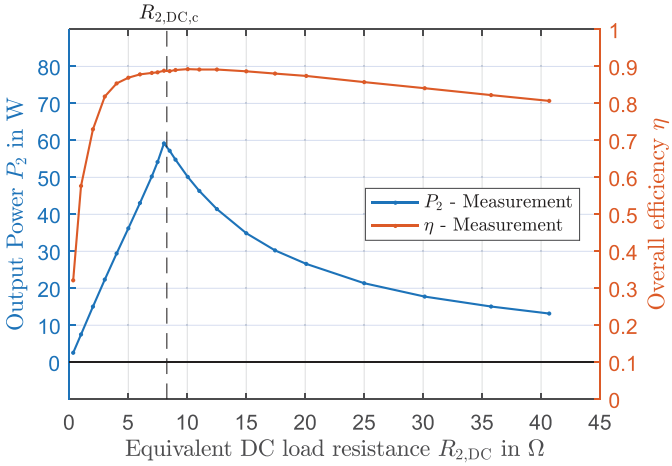

Fig. 18. Output power and overall efficiency of a 1p2p-system; measured values.

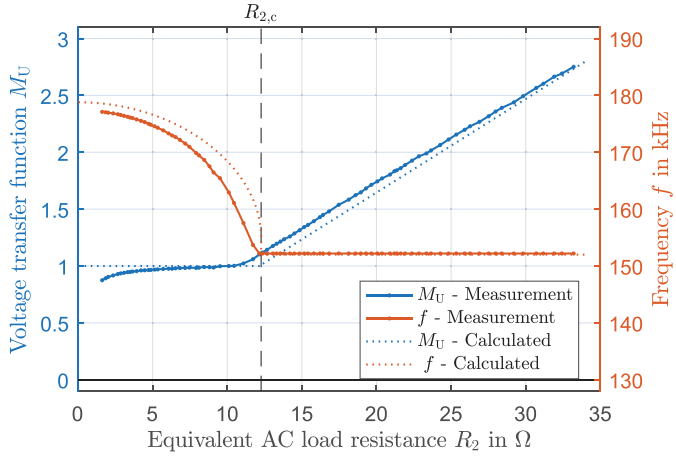

Fig. 19. Voltage transfer function and frequency of a 1s2s-system; calculated versus measured.

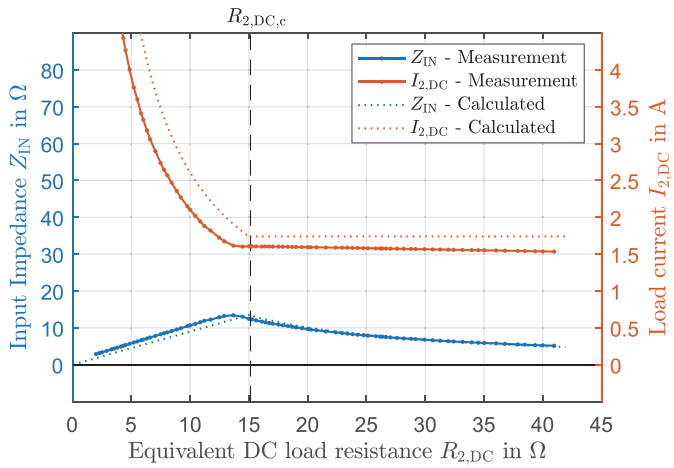

Fig. 20. Input impedance and output current of a 1s2s-system; calculated versus measured.

All figures show a deviation between the measured and calculated values. The reasons for the deviation are, among others, losses in the choke, which is used for the royer converter. Not considered in the calculation are further losses in rectifier, core and litz wire as well as other not mentioned losses. Nonetheless the calculation of Section III-C is very useful to design this system. In consequence of dimensioning the output power to 75 W the constant voltage power supply has its operation point on the right side of $R_{2,DC,c}$ close the maximum of efficiency.

B. 1s2s-Compensated System

In contrast to the constant voltage power supply presented in Section VI-A, the designed charging unit for a battery system is measured and compared to the calculated values in this section. The three Figs. 19–21 present the measurement with the same parameters as with the 1p2p-system before.

The deviations between calculated and measured data are higher compared to the 1p2p-system. A first major difference is, that the 1s2s-system is not operated in an auto-resonant mode, since it is not possible with the used full-bridge inverter showed in Fig. 15 without further controlling systems. By virtue of this, the frequency was set manually during the measurement and it would be more accurate when this process is automated. The second difference is the used full bridge passive rectifier, which has high losses while operated with a low voltage as it was done in this case. Compared to the designed 24 V output voltage, the voltage drop over the used SiC–Schottky diodes is about 10% in the area of the characteristic resistance. The influence is getting smaller with a higher load resistance due to higher output voltage. Based on this, in this special setup the efficiency is higher on the right side of the characteristic resistance.

To complete the measurement an automated frequency- and load-resistance sweep was done with a test bench. Fig. 22 shows the 3D plot of the measured voltage transfer function over the sweep. With the mapped calculated resonant frequencies, the possible resonant operating points are visible.

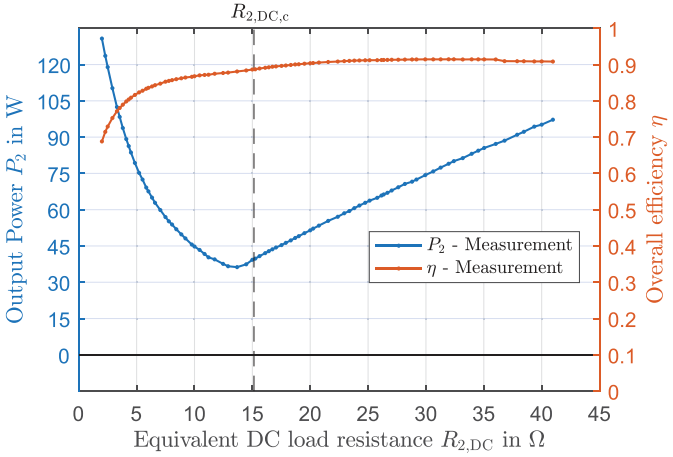

Fig. 21. Output power and overall efficiency of a 1s2s-system; measured values.

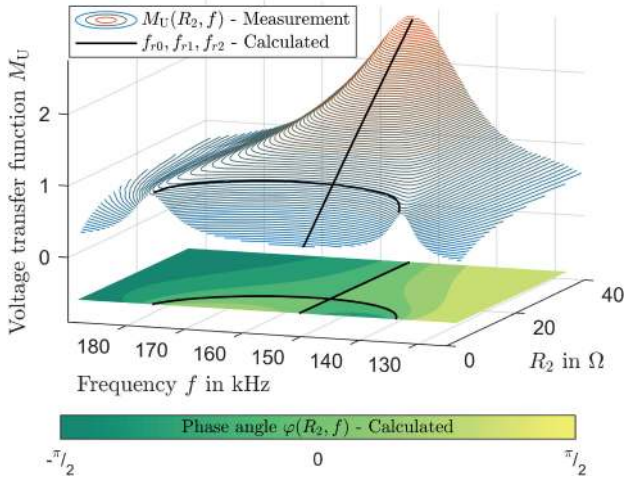

Fig. 22. 3D view of Fig. 19, measured voltage transfer function over frequency and equivalent load resistance shown with the mapped calculated resonant frequencies of a 1s2s-system; below calculated phase angle with resonant frequency.

VII. Conclusion

This contribution contains analytically derived equations that describe the behavior of a CET-system with respect to the various reactive power compensation topologies. It is shown that the knowledge of a particular system behavior contributes to the selection of a suitable reactive power compensation. Starting with the coil system, which is simulated in FEM, the magnetic parameters are acquired for the design process. These parameters are used to calculate the winding numbers of the inductances L_1 and L_2. Furthermore, the influence of harmonics arising due to rectangular voltage or current is analyzed. If the coupling factor is smaller than $k < 0.5$, the harmonics can be neglected for the design procedure. In this case, inverter and rectifier have no impact on the system design. All factors contribute well to the design of a contactless energy transfer system, which is validated in two experimental setups.

References

[1] J. Dai and D. C. Ludois, "A survey of wireless power transfer and a critical comparison of inductive and capacitive coupling for small gap applications," *IEEE Trans. Power Electron.*, vol. 30, no. 11, pp. 6017–6029, Nov. 2015.

[2] D. Schedler, *Kontaktlose Energieübertragung: Neue Technologie für mobile Systeme* (series Die Bibliothek der Technik). Landsberg/Lech: Verl. Moderne Industrie, vol. 321, 2009.

[3] E. Waffenschmidt, "Wireless power for mobile devices," in *Proc. IEEE 33rd Int. Telecommun. Energy Conf.*, 2011, pp. 1–9. [Online]. Available: http://ieeexplore.ieee.org/stamp/stamp.jsp?arnumber=6099840

[4] S. Li and C. C. Mi, "Wireless power transfer for electric vehicle applications," *IEEE J. Emerg. Sel. Topics Power Electron.*, vol. 3, no. 1, pp. 4–17, Mar. 2015.

[5] P. Sergeant and A. V. D. Bossche, "Inductive coupler for contactless power transmission," *IET Elect. Power Appl.*, vol. 2, no. 1, pp. 1–7, Jan. 2008.

[6] G. A. Covic and J. T. Boys, "Inductive power transfer," *Proc. IEEE*, vol. 101, no. 6, pp. 1276–1289, Jun. 2013.

[7] J. Huh, S. W. Lee, W. Y. Lee, G. H. Cho, and C. T. Rim, "Narrow-width inductive power transfer system for online electrical vehicles," *IEEE Trans. Power Electron.*, vol. 26, no. 12, pp. 3666–3679, Dec. 2011.

[8] F. Musavi and W. Eberle, "Overview of wireless power transfer technologies for electric vehicle battery charging," *IET Power Electron.*, vol. 7, no. 1, pp. 60–66, Jan. 2014.

[9] C. Y. Huang, J. T. Boys, G. A. Covic, and M. Budhia, "Practical considerations for designing IPT system for EV battery charging," in *Proc. IEEE Veh. Power Propulsion Conf.*, Sep. 2009, pp. 402–407.

[10] H. H. Wu, A. Gilchrist, K. Sealy, P. Israelsen, and J. Muhs, "A review on inductive charging for electric vehicles," in *Proc. IEEE Int. Elect. Mach. Drives Conf.*, May 2011, pp. 143–147.

[11] M. Zimmer, J. Heinrich, and N. Parspour, "Self-oscillating power converter for an inductive charging system," in *Proc. Power Electron. Conf. Intell. Motion, Renewable Energy Energy Manage.*, Nuremburg, Germany, May 14–16, 2013, vol. 1, pp. 366–372.

[12] K. Knaisch and P. Gratzfeld, "Comparison of magnetic couplers for inductive electric vehicle charging using accurate numerical simulation and statistical methods," in *Proc. 5th Int. Elect. Drives Prod. Conf.*, Sep. 2015, pp. 1–10.

[13] K. Knaisch, M. Springmann, and P. Gratzfeld, "Comparison of coil topologies for inductive power transfer under the influence of ferrite and aluminum," in *Proc. 11th Int. Conf. Ecological Veh. Renewable Energies*, Apr. 2016, pp. 1–9.

[14] M. P. Kazmierkowski and A. J. Moradewicz, "Unplugged but connected: Review of contactless energy transfer systems," *IEEE Ind. Electron. Mag.*, vol. 6, no. 4, pp. 47–55, Dec. 2012.

[15] N. Parspour, J. Heinrich, P. Seitz, and M. Zimmer, "Development of positioning tolerant inductive charging systems for electric vehicles," in *Proc. 3rd Int. Elect. Drives Prod. Conf.*, Nuremburg, Germany, Oct. 29–30, 2013, pp. 426–430.

[16] D. C. Hamill, "Gyrator-capacitor modeling: A better way of understanding magnetic components," in *Proc. 9th Annu. Conf. Appl. Power Electron. Conf. Expo.*, Feb. 1994, vol. 1, pp. 326–332, .

[17] D. Maier, J. Heinrich, M. Zimmer, M. Maier, and N. Parspour, "Contribution to the system design of contactless energy transfer systems," in *Proc. IEEE Int. Power Electron. Motion Control Conf.*, Sep. 2016, pp. 1008–1013.

[18] M. Zimmer, J. Heinrich, and N. Parspour, "Design of a 3 kW primary power supply unit for inductive charging systems optimized for the compatibility to receiving units with 20 kW rated power," in *Proc. 4th Int. Elect. Drives Prod. Conf.*, 2014, pp. 1–5. [Online]. Available: http://ieeexplore.ieee.org/stamp/stamp.jsp?arnumber=6984415

[19] L. Bright and G. Howard, "Electrical inverter circuits," U.S. Patent 2 783 384, Feb. 1957. [Online]. Available: http://www.google.com/patents/US2783384

[20] J. Rehrmann, "MOSFET/IGBT-Oszillatorschaltung für parallelgespeiste Leistungsoszillatoren," German Patent DE202 007 011 745, 2007.

[21] M. Maier, D. Maier, M. Zimmer, and N. Parspour, "A novel self oscillating power electronics for contactless energy transfer and frequency shift keying modulation," in *Proc. Int. Symp. Power Electron., Elect. Drives, Automat. Motion*, Jun. 2016, pp. 67–72.

David Maier was born in Bühl, Germany, on November 7, 1990. He received the graduate degree from the Secondary School, Sasbach, Germany, the bachelor's degree from the Cooperative State University of Stuttgart, Stuttgart, Germany, and the master's degree in electromobility from the University of Stuttgart, Stuttgart, in December 2015.

Since 2016, he has been with the Institute of Electrical Energy Conversion, University of Stuttgart, Stuttgart. His research interests include inductive charging of electric vehicles.

Jörg Heinrich was born in Delmenhorst, Germany, on March 16, 1974. He received the graduate degree from the Secondary School, Oldenburg, Germany, and the Diplom-Ingenieur degree in electrical engineering from the University of Bremen, Bremen, Germany, in 2008.

Since 2008, he has been with the Institute of Electrical Energy Conversion, University of Stuttgart, Stuttgart, Germany. His research interests include coil design for inductive charging applications.

Marco Zimmer was born in Ludwigsburg, Germany, on June 20, 1982. He received the Diplom-Ingenieur degree in electrical engineering from the University of Stuttgart, Stuttgart, Germany, in November 2010. He is currently working toward the Ph.D. degree in electrical engineering at the University of Stuttgart, Stuttgart.

His research interests include inductive charging for electric vehicles.

Marcel Maier was born in Heidelberg, Germany, on June 26, 1986. He received the graduate degree from the Secondary School, Sindelfingen, Germany, and the Diplom-Ingenieur degree in electrical engineering from the University of Stuttgart, Stuttgart, Germany, in August 2012.

Since 2012, he has been with the Institute of Electrical Energy Conversion, University of Stuttgart, Stuttgart. His research interests include rotating contactless energy transfer systems for electrical excited synchronous machines.

Nejila Parspour received the master's degree in electrical engineering, in 1991, and the Ph.D. (summa cum laudae) degree, in 1995, both from Technical University of Berlin, Berlin, Germany.

She is currently a Professor of electrical energy conversion with the University of Stuttgart, Stuttgart, Germany, and the Head of the Institute of Electrical Energy Conversion, Stuttgart, Germany. Before joining the University of Stuttgart, she collected five years of industrial experience at Philips and six years of scientific experience at the University of Bremen. Her research and teaching activities include the field of electrical machines and drives with a focus on machine designs and in the field of contactless energy transfer with a focus on inductive charging systems.